Bioinspiration & Biomimetics

PAPER

RECEIVED
25 November 2025

REVISED
17 April 2026

ACCEPTED FOR PUBLICATION
29 April 2026

PUBLISHED
21 May 2026

Fur roughness, density, and length reduce raindrop penetration of mammalian pelts

Gene Patrick S Rible, John M Wylie, Braeden K Elbers, David Job Dooley, Cora L Thomas and Andrew K Dickerson*

Department of Mechanical, Aerospace and Biomedical Engineering, University of Tennessee, Knoxville, TN, United States of America
* Author to whom any correspondence should be addressed.

E-mail: dickerson@utk.edu

Keywords: rainfall, capillarity, physiology, fur, thermoregulation

Supplementary material for this article is available online

Abstract

This experimental work explores the relationship between the properties and structure of mammalian fur from different habitats and the depth of water drop penetration when impacted in succession. For most mammals, water penetration depth reaches a saturation point, beyond which it no longer increases, creating a dry insulating air layer near the skin regardless of repeated water impacts. To understand this phenomenon, we define several dimensionless quantities representing fur macro-properties, such as guard hair and underfur densities, guard hair and underfur lengths, contact angles, and equivalent diameters. Additionally, we examine microscopic properties such as the aspect ratio and roughness of individual fiber scales. We establish connections between these macro- and microscopic characteristics, the thickness of the dry zone, the depth of water penetration, and the rate at which penetration depth decays exponentially. Our results show that the distal diameter influences the rate at which the penetration depth of water decays with additional impacts. Generally, a higher pelage density, larger guard hair diameter, and increased fur roughness contribute to a thicker dry zone. Using digital microscopy, we confirm that mammalian guard fur is hydrophilic, resisting dynamic water penetration, whereas the finer and denser underfur is hydrophobic, resisting static penetration. This dual-layer structure allows mammals to resist wetting during a heavy rainfall.

1. Introduction

Mammalian fur has two layers: guard hair and underfur. Unlike humans, mammals do not have umbrellas and impervious raincoats to keep them warm and dry during heavy rainfall. Evolution has bequeathed mammals with various body temperature regulation strategies informed by their environment and physiology [1]. Semi-aquatic mammals possessing little to no underfur, such as sea lions and walruses, use blubber as thermal insulation [2–4]. Others rely on the extreme packing density of fur to trap an insulating air layer that is stable during submersion [1–4]. Some mammals possess only one layer of fur. For instance, large-bodied mammals in hot environments have sparse hair to increase heat loss and lack a clear distinction between underfur and guard hairs [5]. Guard hairs are longer and fatter than the denser, downy underfur hairs. [3, 4, 6–8]. The fur is organized into bundles consisting of one guard hair surrounded by underfur and varies among mammals [2].

Semi-aquatic mammals such as the beaver, sea otter, and mink all have coronal scale structures. Coronal scales completely encircle the hair cuticle and are stacked up the cuticle towards the distal end of the hair shaft [9–12]. Terrestrial mammals such as moose, zebra, and gray wolf all have imbricate scale structures where the scales are laid in an overlapping pattern to decrease the wettability of the hairs [13]. Although individual imbricate scales do not encircle the hair cuticle entirely, the multitude of these scales in the pattern provides the hair with full coverage [13]. Spinous scales, observed in mammals such as cats, seals, and minks, do not individually encircle the cuticle but are laid in a petal-like overlapping pattern, providing coverage similar to the imbricate pattern. [12, 14]. Such microscopic properties of mammalian fur produce physicochemical forces by which the hairs

interact with each other. Surface interactions of the hairs passively contribute to the anti-fouling properties of mammalian fur by trapping a layer of air on the fur to block out water and through the surface topography affecting the way water accumulates on a surface [15–17].

We hypothesize that nano- and micro-structures influence the water-resistant property of most mammalian furs, similar to how the surface topography of the lotus leaf makes it superhydrophobic [16]. The medulla, the core of the hair shaft beneath the cuticle, has a scale-like structure that causes the fur fibers to interlock with each other. It is responsible for the ability of semi-aquatic mammals to prevent contact of water with mammalian skin [4, 18]. This interlocking mechanism works in conjunction with the horizontal orientation of fur along the mammalian skin, which points to the posterior of the body [19]. From previous works, we know that horizontally-oriented fibers increase water drop spreading across a mammal pelage, reducing penetration, whereas vertical fibers restrict drop spreading, promoting penetration [20, 21].

Previous studies have investigated the presence of an air layer in some semi-aquatic mammals when fully or partially submerged in water [1, 2, 4]. When fully submerged, air is trapped between the hair and the pelt, with hydrostatic and hydrodynamic pressures holding the hair in place. When swimming on the surface, the air layer is connected to the atmosphere [1]. These works describe the mechanisms by which mammals maintain this air layer and introduce a ratio that characterizes the ability of fur to retain air upon initial contact with water [1]. The air layer is only preserved if the physicochemical properties of the fur-water boundary, influenced by key factors such as wettability [20], hair size, length, roughness, density, and arrangement, are sufficient to resist water pressure [2, 22]. To retain the guard layer, the guard hairs must be flexible to bend and trap air, yet stiff enough to resist collapse under hydrodynamic pressure. [2] The required stiffness is closely related to mammal size, as larger mammals experience greater hydrodynamic forces [1]. The water pressure acting on a swimming mammal is directly influenced by its size and speed. Larger mammals tend to swim faster, following the scaling law [23, 24] $v \propto L^{1/2}$, and as a result, they experience greater hydrodynamic pressure, which scales [25] as $P \propto v^2$. Whereas the ability of mammalian fur to resist water penetration through pressure when submerged has been widely studies, to our knowledge, there is a scarcity of published work on the ability of mammalian fur to resist penetration through impact momentum during rainfall.

In our previous works, we have fabricated fur-like fiber arrays with tunable properties to isolate the parameters that govern water repellency and air retention in mammalian fur during rainfall [20, 21, 26, 27]. Horizontally oriented fibers are better at resisting liquid penetration than vertical fibers [21], a finding that provides insights into the orientation of the fur of mammals living in different environments from deserts to rainforests. When the fiber arrays are horizontally oriented, hydrophilic fibers resist the penetration of impacting drops, whereas hydrophobic fibers prevent wicking of static drops [20]. From such findings, we hypothesized that mammalian guard hairs are hydrophilic, serving to absorb the initial kinetic energy of raindrops and channel the liquid downward toward the underfur, which would be hydrophobic, serving to prevent wicking of close-to-static liquid from the guard fur. We confirm such a hypothesis in this work as discussed in section 3. In sequential drop impacts, a second drop penetrates less than the first drop [26]. At high Weber numbers, the second drop produces almost zero additional penetration. Thus, we hypothesize the existence of a dry zone where penetration eventually ceases and no additional drops reach the mammalian skin—a major point of investigation in this work.

Although informative, synthetic fur-like structures do not capture the full diversity of densities, thickness, and combinations of morphologies found in actual mammalian fur. Mammalian furs are generally much finer and denser than the fibers we are able to manufacture and thus provide a regime that cannot be tested with synthetic, tunable samples. The limited fidelity of the shapes and structures that can be achieved in artificially fabricated fur samples makes them insufficient to directly confirm the presence or persistence of insulating air layers in furry mammals. This study utilizes biological fur samples which have densities that are far greater than what can be manufactured in lab.

In this work, we explore the influence of various properties of actual mammalian fur on the penetration depth of sequential impacting drops. Our work aims to simulate rain in a controlled manner using sequential drops and further prove the existence of a dry zone above the skin of most mammals during a heavy rainfall. We identify how the dry zone changes for mammals native to different habitats as the number of drops is increased. We show that the depth of liquid penetration, dry zone thickness at saturation, and rate of saturation relative to the number of drops are correlated with the physical properties of mammalian fur. Our findings may prove useful in creating fur-like surfaces that resist water penetration or hairy surfaces that capture moisture and rain [28].

Beyond biological fur studies, several of our recent works have used idealized synthetic fiber arrays to isolate the physical mechanisms governing drop-fiber interactions. Synthetic horizontally oriented fibers [20], vertically oriented arrays [21], and sequential-impact studies [26] have clarified how density, spacing, and wettability regulate spreading, capillary retention, and penetration. Most recently,

we showed that fiber cross-sectional shape alone influences penetration: circular cross-sections suppress lateral spreading and deepen penetration even when the fibers are hydrophilic [27]. However, such idealized arrays cannot replicate the hierarchical roughness, extreme packing densities, mixed guard-underfur layers, or natural tapering found in real pelage. The present study fills the gap by showing that actual mammalian pelts exhibit a limiting penetration depth and a persistent dry insulating zone across species, behaviors not captured in synthetic arrays. In this work, we connect synthetic-array physics to the complex, evolved fluid-fur architectures of mammals.

2. Methods

2.1. Experimental setup

We measure the penetration depth into fur after the impact of $n = 2, 4, 7,$ and 10 drops with a diameter of 2.86 ± 0.13 mm from a fixed height to achieve a velocity of $5.48 \pm 0.015\,\mathrm{m\,s^{-1}}$, as shown in figure 1. The drops are released at one-second intervals, which allows each drop to reach a quasi-steady state before the next impact [20, 29] and ensures that neither evaporation [30] nor wicking [31] significantly alters the retained liquid. The number of trials for each value of n is $N = 3$. Upon release from the needle, a shielding tube minimizes ambient airflow effects and ensures that all drops impact the same location on the fur. Following drop impact, two 0.64 mm diameter needles spaced 1 mm apart are inserted through a hole in the base of the fur pelt and translate upward at $4.16 \pm 0.05\,\mathrm{mm\,s^{-1}}$ until encountering water, controlled using a linear actuator driven by an Arduino Mega 2560 microcontroller, resulting in a measurement precision of 10 μm. Contact with water closes an electrical circuit and halts the needle motion. The displacement of the needles, recorded by a digital caliper rigidly coupled to the actuator, gives the penetration depth from the skin to the liquid front.

To ensure both accuracy and repeatability, the zero position of the needles is re-established before each trial by gently bringing the tips into contact with the skin side of the pelt, providing a consistent reference plane. The needles are guided so that they translate normal to the pelt surface, and the rigid coupling between the caliper and actuator ensures that the measured displacement corresponds exactly to the penetration depth. All experiments were performed using the same drop generator, needle geometry, release height, and timing protocol so that the drop diameter D_0 and impact velocity U remained constant within the stated uncertainties. The drops were always released vertically and shielded from air currents to maintain consistent impact location and trajectory, and the fur samples were clamped to a rigid support to prevent motion or sagging during repeated impacts. For each species and each value of n, we conducted three independent trials and report the mean penetration depth with error bars representing one standard deviation. The small scatter in the data-typically comparable to or smaller than the symbol size in the plots-demonstrates excellent repeatability of the experimental protocol.

The chosen drop parameters are intended to represent practical rainfall conditions in a controlled and repeatable way. The drop diameter $D_0 = 2.86 \pm 0.13$ mm lies within the typical range of raindrop sizes encountered in moderate to heavy rain, and the release height is selected so that the impact velocity $U = 5.48 \pm 0.015\,\mathrm{m\,s^{-1}}$ is comparable to the terminal velocity of millimeter-scale raindrops, but not all raindrops. The one-second interval between drops allows each impact to relax toward a quasi-steady configuration before the next drop arrives, mimicking a locally intense sequence of impacts rather than an isolated drop. In addition, all drops are released normal to the fur and shielded from ambient air currents by the tube, so the impact direction and speed are consistent from trial to trial. Concentrating the sequential impacts at a single location on the pelt represents a conservative, worst-case scenario for local wetting and provides a practical upper bound on penetration depth under sustained rainfall.

2.2. Fur profiling

Unwashed, non-taxidermied cat fur (*Felis catus*) was collected from freshly dead cats donated to the College of Veterinary Medicine of the University of Tennessee, Knoxville. Taxidermied, scrap fur pelts were donated by Broderick Head's Taxidermy in Bremen, GA in 2010. These same fur samples were used in a number of previous works [15, 32, 33]. We use a subset of these taxidermied pelts from a zebra (*Equus quagga*), gray wolf (*Canis lupus*), moose (*Alces alces*), beaver (*Castor canadenis*), mink (*Neovison vison*), and sea otter (*Enhydra lutris*) in this study. Mammal hair tapers in width from the base. We identify three important hair cross-sections: the proximal section, the thickest cross-section (in micrometers) which is the base of the hair shaft and in contact with the mammalian skin; the medial section which is the center cross-section along the length of the hair; and the distal section, the thinnest cross-section (in nanometers) which is at the tip of the hair. Approximately 1.10 mm of the distal and proximal ends of the hair are hot-glued to pull the hair taut. We orient the hair with the distal end pointing away from the base. We fill a 7.6 cm square glass container with distilled water and place the hair vertically into distilled water as shown in figure 2. We use a Keyence VHX-7000 series digital microscope to measure the receding θ_r, equilibrium θ_e, and advancing θ_a wetting angles at 100x magnification. The inside of the glass container is coated with superhydrophobic Glaco to reduce the meniscus that obscures the view of the contact angle. An electronic syringe pump moves water

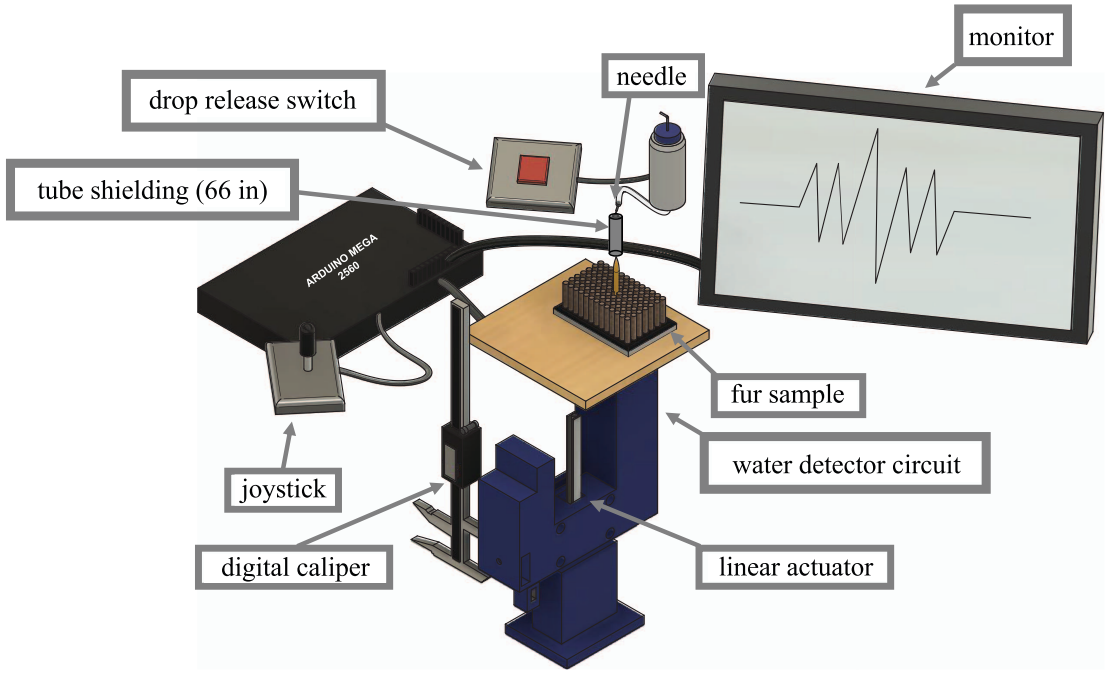

Figure 1. Experimental setup. A number of drops are sequentially dispensed through a needle using the drop release switch to impact mammalian fur samples. Two parallel needles connected to a microcontroller circuit and controlled by a joystick insert through a hole to detect the dry zone in the sample, measured by a digital caliper, and displayed on a computer monitor. Drops are protected from external airflow after release by a tube in order to ensure convergence of drop impact locations in the fur sample.

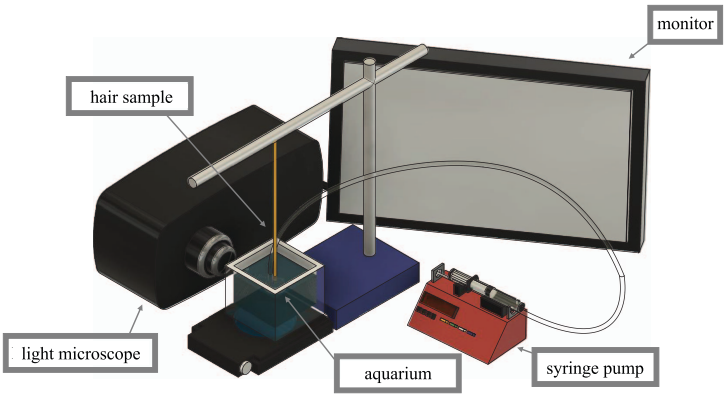

Figure 2. Setup to measure contact angle of guard hair and underfur hair samples. The hair is pulled taut and submerged vertically into an aquarium while a digital light microscope films the contact angle of the drops. Water is pumped into and out of the aquarium by an electronic syringe pump in order to measure the advancing and receding contact angles.

into and out of the container at a steady flow rate to generate advancing and receding contact angles. The contact angles of our pelts samples were taken at the medial section of the guard fur.

Microscope images of the fur samples are shown in figure 3. Measurement of the contact angle is shown in figure 3(a). We use a method published by Koch [34] to obtain cross-section images of a guard fur hair from which we calculate its equivalent diameter. We insert guard hair samples into polyethylene pipettes. The pipette is placed between clean glass microscope slides wiped down with 99% isopropyl alcohol solution, and melted on a hot plate at 30 °C until the pipette morphs into a thin translucent layer encasing the hair. Tweezers are used to eliminate bubbles. An illustration of the method is shown in figure S1 of our supplementary document. The hardened samples are cross-sectioned and imaged with our digital microscope, as shown in figure 3(b). We binarize microscope images of our fur samples using MATLAB. From the binarized images, geometrical measurements of the distal, medial, and proximal regions are made. To measure fur density, we cut $\approx 1\,\text{cm} \times 1\,\text{cm}$ from our fur pelt sample and use hair clippers to shave the fur pelt to 1/16 in. Using a Keyence VHX-7000 series light microscope with

built-in image analysis software, we run a count of the number of circles corresponding to hair fibers for the selected area shown in figure 3(c). We use a Keyence VK-X3000 3D laser scanning confocal microscope to measure the standard deviation line roughness of the samples as shown in figure 3(d). The microscope gives us the depth profile of the scanned surface with a resolution of 0.01 nm. We select three parallel axes along the length of the hair as shown in figure 3(d). We take the root mean square value of the depth the three axes and take the mean as our roughness measurement for the hair sample. For nanoscale details such as the scale type at the distal end of a hair, we use a TM3030 Hitachi tabletop scanning electron microscope.

Guard hairs are the first line of defense of mammals against external forces such as impacting raindrops. Their larger diameter and greater exposure make them more suitable for surface roughness and impact dissipation measurements. Thicker and rougher guard hairs increase the probability of intercepting and dissipating the initial kinetic energy of water droplets through friction before it reaches the underfur [35]. Measurements of equivalent diameter, arithmetic roughness, and standard deviation line roughness are easily obtained for guard hair, but are difficult to obtain for underfur. Underfur, the second layer of defense, functions as a hydrophobic barrier that repels water and traps the insulating air layer. Due to its significantly smaller diameter, higher density, and interweaving structure, underfur is more difficult to isolate and characterize using the same morphological metrics applied to guard hairs. Measurements of underfur diameter and surface roughness are not present in the literature [1, 36]. Previous studies have acknowledged the challenges of obtaining underfur measurements and often exclude detailed underfur surface analyses, opting instead to focus on underfur density and length [2, 19], which are the same underfur measurements we obtain in this work. Variables measured in this work are listed in table 1. The measured values are provided in table S1, along with a corresponding range of typical values reported for mammals. From the micro- and macro-properties of the mammalian guard fur and underfur, we build a model predicting the dry zone thickness within mammalian furs after successive drop impacts.

3. Results

Previous studies using 3D-printed or synthetic arrays have shown that drop penetration dynamics are highly sensitive to fiber cross-section, wettability, spacing, and arrangement. In horizontally oriented synthetic arrays, fibrous wettability dominates spreading and supersurface retention [20]. In vertical arrays, penetration increases because lateral spreading is restricted [21]. Sequential-impact studies revealed an exponential saturation in penetration depth [26]. Most relevant to the present work, our recent study demonstrated that circular cross-sections promote deeper penetration and increased fragmentation by suppressing lateral spreading [27]. In contrast, the biological pelts tested in this work exhibit a limiting penetration depth and maintain a dry insulating zone across species, indicating that natural fur microstructure and hierarchical architecture fundamentally alter the impact-infiltration pathway relative to engineered arrays.

In this work, we allow sequential drops to impact a single spot on mammalian fur pelts and measure the distance from the dry skin to the location of water ingress for various numbers of impacting drops. Mammalian fur is comprised of a thick underfur and longer, straighter guard hairs that protrude outward past the underfur layer [15, 19, 33], as shown in figure 4(a). Guard hairs, which have packing density δ_g, length L_g, and distal diameter d_3 act to dissipate the kinetic energy of falling drops and guide the drops into the underfur layer [20] as illustrated in figure 4(b). A thicker guard hair increases the surface area in contact with water, aiding in the dissipation. Additionally, a rougher surface on the guard hair increases friction and the amount of kinetic energy dissipated before contact with the underfur [37]. Underfur, which has packing density δ_u and length L_u consists of fine hairs weaving together to form a hydrophobic barrier that restricts any static penetration. The dry zone thickness ζ is the normal distance from the mammal skin to the closest water body. As successive drops impact the fur, the ζ decreases. In this work, we show that ζ achieves a steady-state value k_2 and that a steady-state penetration depth k_1 is achieved after enough number of drops have impacted the same neighborhood of the mammalian fur. The dry zone decay rate with respect to the number of drops on a particular impact location is λ. We provide a graphic illustration of the physical manifestation of the time-varying dry zone ζ, the steady-state penetration depth k_1, the steady-state dry zone thickness k_2, and fur thickness L under the impact of successive water drops in figure 4(c).

The scale type of guard fur and underfur hair varies throughout the length of the hair as shown in figure 5. We classify the guard hair scale structure of our mammalian fur samples in table 2. Although the cuticle structure does not always change between the distal, medial, and proximal regions, transitions, when present, are gradual rather than abrupt, as shown in figure 5(a) which shows a transition from the coronal—simple distal to the imbricate—acuminate medial region of a guard hair of a sea otter.

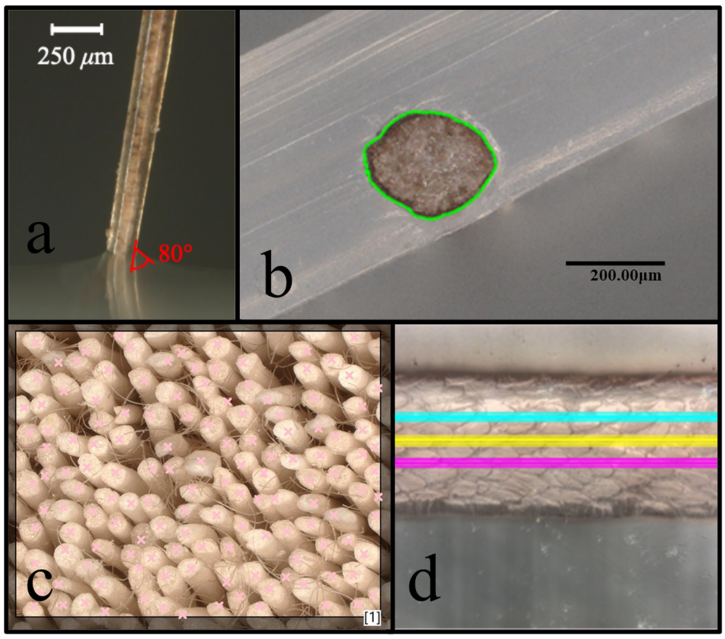

Figure 3. (a) Measuring contact angle using Keyence VHX-7000 series digital light microscope. (b) Calculating the equivalent diameter from a cross-section of mammalian guard hair (outlined in green). (c) Measuring guard hair density using a digital light microscope. The number of hairs (marked by an '*x*') in a known area is counted. (d) Obtaining the root mean square roughness of beaver guard hair along three different lengths (shown in cyan, yellow, and magenta).

Table 1. Nomenclature.

Symbol	Description
L [mm]	Normal distance from skin to outermost edge of mammalian guard fur
L_g [mm]	Guard hair length
L_u [mm]	Underfur hair length
δ_g [mm^{-2}]	Guard hair density
δ_u [mm^{-2}]	Underfur density
d_3 [nm]	Distal diameter of guard hair
$\tilde{r}_g$ [μm]	Standard deviation line roughness of guard hair
θ_e [°]	Equilibrium contact angle
θ_a [°]	Advancing contact angle
θ_r [°]	Receding contact angle
ζ [mm]	Dry zone thickness
L' [mm]	Value of $L = k_1 + k_2$ predicted from model, refer to equation (1)
k_1 [mm]	Saturation depth, refer to equation (4)
k_2 [mm]	Dry zone thickness at saturation, refer to equation (7)
λ	Rate of saturation with respect to number of drops, refer to equation (10)
D_0 [mm]	Drop diameter
U [m s]	Drop impact velocity
ρ [kg m^{-3}]	Liquid density
μ [kg (m·s)$^{-1}$]	Liquid dynamic viscosity
σ [N m^{-1}]	Liquid surface tension
Re	Impact Reynolds number
We	Impact Weber number
Oh	Impact Ohnesorge number

In a previous paper [20], we hypothesized that mammals have a hydrophilic guard fur and hydrophobic underfur in order to optimally resist wetting during rainfall. We confirm such a hypothesis as shown in our receding (θ_r), equilibrium (θ_e), and advancing (θ_a) contact angle measurements listed in table S2 of our supplementary document. We include the guard hair and underfur contact angles of a blue feline domestic cat (*F. catus*), not taxidermied, in addition to the contact angles of the guard hair of our taxidermied pelts. The contact angle and contact angle hysteresis ($\theta_a - \theta_r$) of water on our taxidermied fur samples listed in table S2 did not significantly impact the dry zone layer. We note that no significant difference in contact angle was observed between taxidermied and fresh pelts, suggesting that,

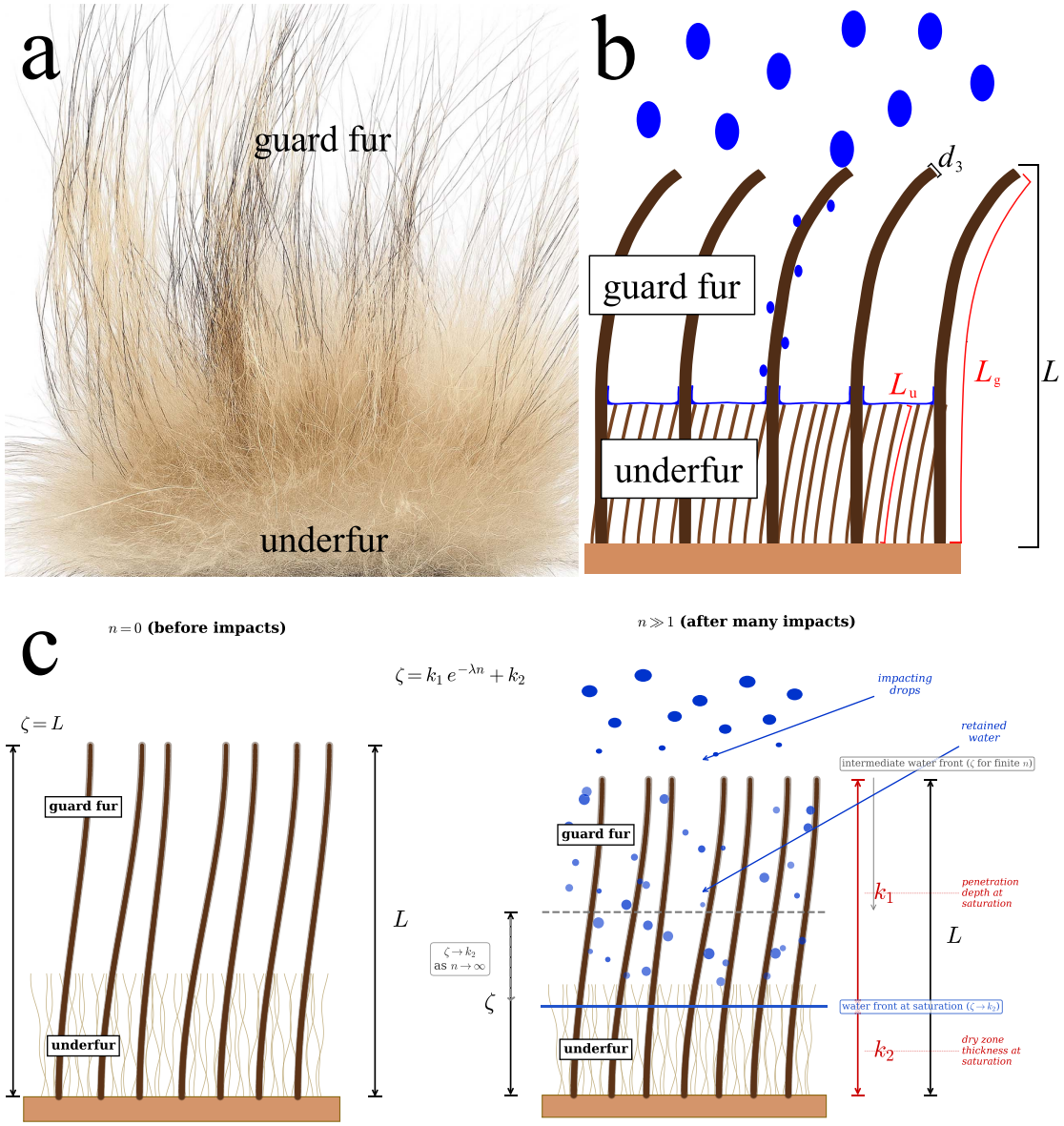

Figure 4. (a) Straighter guard fur of a taxidermied gray wolf pelt protruding outward past the denser underfur at the base. (b) Guard hairs act to dissipate the kinetic energy of falling drops and guide the drops into the underfur layer consisting of fine hairs weaving together to form a hydrophobic barrier that restricts any static penetration. (c) Graphic illustration of the physical manifestation of the time-varying dry zone ζ, the steady-state penetration depth k_1, the steady-state dry zone thickness k_2, and fur thickness L. The left panel shows the dry state before any impacts ($n = 0$). The right panel shows the fur after many impacts ($n \gg 1$). Small blue circles between the guard hairs represent water retained within the fur. Drops above the fur canopy represent incoming impacting drops. The solid blue line marks the water front at saturation ($\zeta \to k_2$ as $n \to \infty$), whereas the dashed line marks an intermediate water front for a finite number of drops n. The dimensionless rate of saturation λ governs how quickly ζ decays toward k_2. An equation is provided for the time-varying dry zone at the bottom of the illustration.

with the possible exception of few mammals such as sheep with a lanolin-covered curvy wool [38], the hydrophobic and hydrophilic nature of a straight guard fur or underfur hair is governed solely by its microstructure rather than any oil or chemical coatings originating from the mammalian skin.

In this section, we demonstrate that the penetration of impacting drops into mammalian fur decays exponentially with the number of drops that impact a common spot. Liquid ingress is resisted by fur. Resistance to penetration is enhanced by fur diameter and density, generally, as expected, but so too by the microscopic roughness of the individual fibers. Liquid ingress depletes the dry zone length ζ, the normal distance between the mammal skin and the maximum liquid penetration depth within the mammal fur. The dry zone thickness for various test furs is plotted against the number of drops in figure 6(a). We took measurements with a zebra pelt but do not include them in the plots because the zebra pelt did not resist penetration of the drops due to its low density and short length. Here, ζ denotes the dry-zone thickness, defined as the normal distance from the skin of the mammal to the maximum liquid

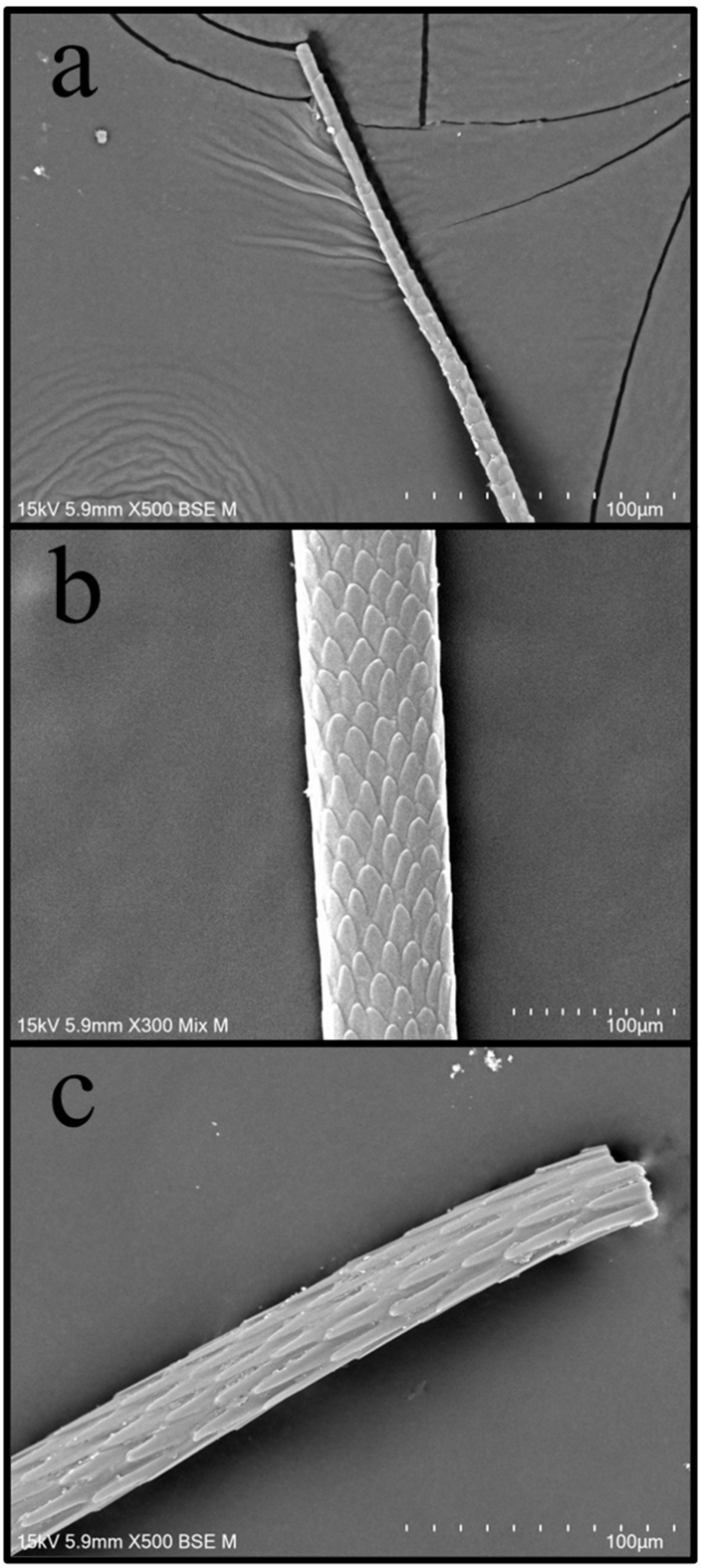

Figure 5. (a) Distal section of sea otter guard hair imaged using a scanning electron microscope, showing coronal—simple pattern transitioning into an imbricate—acuminate pattern towards the medial section. (b) Medial section of sea otter guard hair imaged using a scanning electron microscope, showing an imbricate—acuminate pattern. (c) Proximal section of sea otter guard hair imaged using a scanning electron microscope, showing an imbricate—acuminate pattern.

Table 2. Classification of guard hair scale structures of our mammalian fur samples.

Mammal	Distal scale structure	Medial scale structure	Proximal scale structure
Zebra	Imbricate—flattened	Imbricate—crenate	Imbricate—crenate
Gray wolf	Imbricate—elongate	Imbricate—crenate	Imbricate—crenate
Moose	Imbricate—acuminate	Imbricate—flattened	Imbricate—flattened
Beaver	Imbricate—crenate	Imbricate—crenate	Imbricate—crenate
Mink	Coronal—dentate	Imbricate—acuminate	Imbricate—crenate
Sea otter	coronal—simple	Imbricate—acuminate	Imbricate—acuminate

penetration depth within the fur following n sequential drop impacts. As the number of drops increases, the dry zone thickness decays exponentially. A similar limiting behavior is observed in our previous experiments on artificial horizontally oriented fiber arrays [26]. We propose an exponential decay model that is a function of the number of drops n:

$$\zeta = k_1 e^{-\lambda n} + k_2 \tag{1}$$

where k_1, k_2, and λ are constants. The constant k_1 represents the penetration depth of water at saturation, k_2 is the dry zone thickness at saturation, and λ is the rate at which saturation is reached by adding drops. The exponential form is appropriate because the process satisfies the condition that the rate of change per drop impact is proportional to the remaining difference from a limiting value. Such a behavior is analogous to porous medium filling models, where the filling rate decreases exponentially as the available pore space is occupied [39]. When the array is dry, the first drops can penetrate readily, but as liquid accumulates between fibers, subsequent drops interact with an increasingly saturated structure and an existing 'pool' of liquid. Prior work on drop impacts onto liquid layers shows that a pre-existing film dissipates more impact energy than a dry surface [40], reducing penetration depth per drop. As a result, each additional drop yields a progressively smaller increase in penetration, producing an exponential approach toward a maximum penetration depth. Model fits to our experimental data in figure 6(a) carry correlation coefficients with $R^2 = 0.9776 - 0.9996$. Results are grouped by color to represent different habitats and classifications, such as semi-aquatic and terrestrial mammals in different habitats. If the model proposed in equation (1) is appropriate, $k_1 + k_2 \approx L$, where L is the normal distance from the skin to the extents of the guard fur layer. We plot $k_1 + k_2$ against L in figure 6(b). The points cluster about the $k_1 + k_2 = L$ line to within 4.5 mm of error along the horizontal or vertical axis. The plot is zoomed which can make the datapoints appear to deviate from the theoretical line more than they actually do. The values of fitting constants extracted from equation (1) allow us to examine how these saturation points change with the physical properties of fur pelts. The error bars in the penetration depth data represent the standard deviation over three independent trials, and are generally smaller than the symbol size, confirming the repeatability of the measurement. The error bars in figure 6(a) represent one standard deviation over three independent trials for each species and n, and are generally smaller than or comparable to the symbol size, further confirming the repeatability of the measurements.

Based on the fur macro- and micro-properties, we propose non-dimensional groups that correlate with the dry zone thickness coefficients k_1, k_2, and λ. The process of arriving at these non-dimensional groups is discussed in section 4. Although the non-dimensional groups are not equal to the experimental coefficients shown in figure 6(a), the experimental coefficients follow a monotonic trend with the non-dimensional groups that we proposed as shown in figures 6(c)–(e). The error bars in figures 6(c)–(e) represent the standard deviation of the non-dimensional groups.

4. Discussion

The connection between the macro-scale and micro-scale fur characteristics is made explicit through the dimensionless groups constructed using the Buckingham-Pi theorem. These groups combine the primary geometric variables (δ_g, δ_u, L_g, L_u, d_3) with a microscopic descriptor of surface topology ($\tilde{r}_g$), forming unified parameters that correlate with the saturation depth k_1, dry-zone thickness k_2, and saturation rate λ. At the macro scale, guard hair and underfur densities, lengths, and diameters determine the effective pore geometry and the amount of fur material interacting with an impacting drop. At the micro scale, roughness and cuticle-scale patterning influence viscous dissipation, frictional drag, wettability, and the degree of interlocking between neighboring fibers. By combining these effects, the dimensionless groups capture the coupled geometric and interfacial mechanisms that govern drop penetration. Such an integration explains why the exponential decay coefficients vary monotonically with the groups: penetration depth and dry-zone thickness are constrained by bulk geometric properties, whereas the saturation rate depends sensitively on microscopic dissipation and capillary interactions. Thus, the observed decay behavior arises from a multiscale

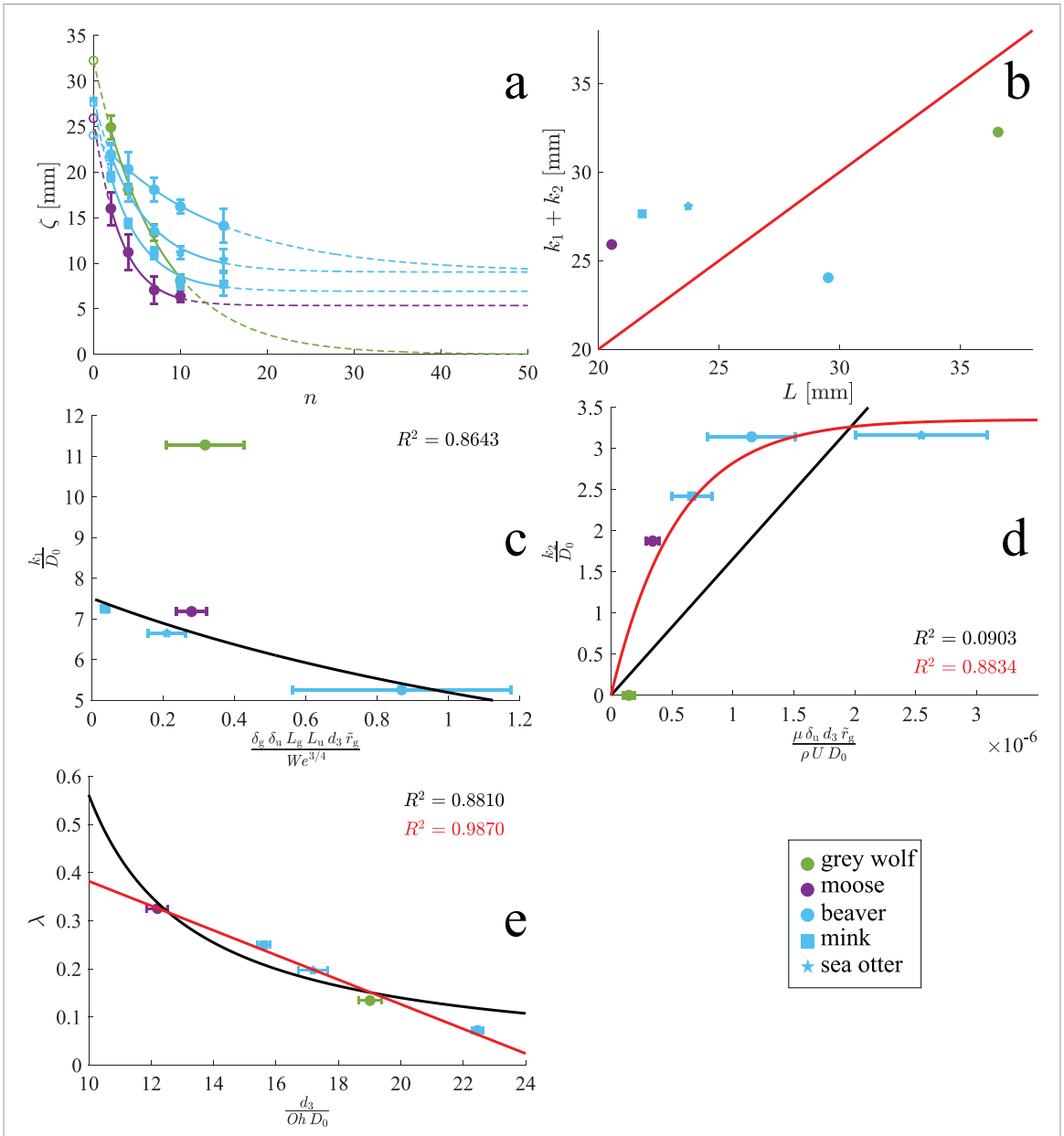

Figure 6. (a) Plot of dry zone thickness ζ versus the number of drops n. (b) Plot of the model-predicted normal distance of the outermost edge of mammalian guard fur layer from the skin $k_1 + k_2$ versus the measured normal distance L. (c) Plot of the model-predicted penetration depth at saturation k_1 versus the reciprocal of the functional group in equation (4). Black fit: $y = c/(x - x_0)$; $c = 15.37$, $x_0 = -2.05$. Gray wolf data is excluded from data fitting in (c) for reasons explained in section 4. (d) Plot of the model-predicted dry zone thickness at saturation k_2 versus the functional group in equation (7). Black fit: $y = cx$, $c = 1.65 \times 10^6$. Red fit: $y = c_1 - c_1 e^{-c_2 x}$; $c_1 = 3.30$, $c_2 = 2.02 \times 10^6$. (e) Plot of the model-based rate of saturation λ versus the reciprocal of the functional group in equation (10). Black fit: $y = c/(x - x_0)$; $c = 1.86$, $x_0 = 6.68$. Red fit: $y = c_1 x + c_2$, $c_1 = -0.03$, $c_2 = 0.64$.

mechanism rather than from either macro- or micro-scale features alone.

Intuitively and through previous experiment [20, 21, 26, 27] we expect the penetration depth at saturation to decrease as guard and underfur density and length increase. Further, we expect larger and rougher hairs [37, 41] to reduce penetration. Using the Buckingham Pi theorem, we find a dimensionless group combining relevant fur properties into a single functional group of fur and drop parameters that is correlated with k_1, k_2, and λ. The dimensional variables that define our problem are the liquid density ρ, drop impact velocity U, drop diameter D_0, liquid dynamic viscosity μ, liquid surface tension σ, liquid penetration depth k_1, guard fur density δ_g, underfur density δ_u, guard hair length L_g, underfur hair length L_u, guard hair distal diameter d_3, and guard hair standard deviation line roughness $\tilde{r}_g$. The guard hair distal diameter d_3 is an equivalent diameter defined as $D = 4A/P$ where A is the cross-sectional area of the guard hair, and P is the perimeter of the guard hair. We define $\tilde{r}_g = \sqrt{1/n \sum_{i=1}^{n} (x_i - \bar{x})^2}$, where n is the number of samples, x_i is the height of each sample along the

sampling length, and $\bar{x}$ is the average height of all samples in the sampling length, with the sampling length constructed parallel to the length of the hair as shown in figure 3(d).

We propose the following Π terms: $\Pi_1 = \mu/\rho D_0 U$ which is the reciprocal of the Reynolds number Re, $\Pi_2 = \sigma/\rho D_0 U^2$ which is the reciprocal of the Weber number We, $\Pi_3 = k_1/D_0$, $\Pi_4 = k_2/D_0$, $\Pi_5 = \lambda$, $\Pi_6 = \delta_g {D_0}^2$, $\Pi_7 = \delta_u {D_0}^2$, $\Pi_8 = L_g/D_0$, $\Pi_9 = L_u/D_0$, $\Pi_{10} = d_3/D_0$, and $\Pi_{11} = \tilde{r}_g/D_0$. From our previous work on fur-like fiber arrays [20, 21, 26, 27], we know that the penetration depth decreases as the impact Weber number increases, with a leading-order scaling $k_1/D_0 \propto We^{-3/4}$, derived by conservation of energy in our previous work [20], and is reduced by increasing guard and underfur density. Moreover, the penetration depth is reduced by dissipation of the kinetic energy of the impacting drop, which is promoted by a greater distal diameter and greater surface roughness of the guard hairs, and by longer fibers that tend to lie more horizontally due to the weight of the cantilevered hairs, improving resistance to liquid penetration [20, 21]. In terms of the Π groups, this implies that the dimensionless penetration depth $\Pi_3 = k_1/D_0$ must be a decreasing function of Π_6, Π_7, Π_8, Π_9, Π_{10}, and Π_{11} and an increasing function of $\Pi_2^{-3/4}$ (i.e. $We^{-3/4}$). For the limited number of species considered here, rather than attempting to identify a fully general multivariate function, we assume a separable power-law dependence,

$$\Pi_3 \propto \Pi_2^{\alpha_2}\Pi_6^{\alpha_6}\Pi_7^{\alpha_7}\Pi_8^{\alpha_8}\Pi_9^{\alpha_9}\Pi_{10}^{\alpha_{10}}\Pi_{11}^{\alpha_{11}}, \tag{2}$$

and choose exponents such that (i) $\alpha_2 = -3/4$ to recover the previously observed $We^{-3/4}$ scaling, and (ii) $\alpha_6, \alpha_7, \alpha_8, \alpha_9, \alpha_{10}, \alpha_{11} > 0$ so that increases in density, length, diameter, and roughness reduce Π_3. This leads to the scaling

$$\Pi_3 \sim \frac{\Pi_6\Pi_7\Pi_8\Pi_9\Pi_{10}\Pi_{11}}{\Pi_2^{3/4}}, \tag{3}$$

which, upon substitution of the definitions of the Π groups, yields

$$\frac{k_1}{D_0} \sim \left(\frac{\delta_g\delta_u L_g L_u d_3 \tilde{r}_g}{We^{3/4}}\right)^{-1}. \tag{4}$$

A plot of k_1 versus $\delta_g\delta_u L_g L_u d_3 \tilde{r}_g/We^{3/4}D_0$ is shown in figure 6(c). Gray wolves shed from April to June and lose their thick winter coat [42]. Our gray wolf pelt stands out as an outlier in figure 6(c) with a very high penetration depth at saturation due to a sparse guard fur and underfur during summer months, and has thus been excluded from subsequent data fitting. In mammals with a non-zero dry zone thickness at saturation k_2, k_1 is a function of δ_g, d_3, L_g, $\tilde{r}_g$,δ_u, and We. In cases where $k_2 = 0$, k_1 is solely determined by L_g and We. For instance, the gray wolf, with long guard hairs, has a high k_1 value of 32.26 mm, whereas the zebra, with shorter guard hairs, has a lower $k_1 = L$ value of 1.74 mm, and both mammals have $k_2 = 0$.

In our previous study, we find that the dry zone is achieved through dissipation of kinetic energy by the guard hair [20, 26] which is promoted by a higher d_3 and r_g, and a dense, hydrophobic underfur which is more effective at preventing wicking with higher δ_u. A previous study has defined a critical pressure $P_{crit} \sim \delta_u d_3$ that, if overcome, the physical properties of the fur-water boundary will cause the dry zone to collapse [1] when the mammal is partially or fully submerged. In the case of falling raindrops, the pressure that the fur has to withstand comes from the dynamic pressure as opposed to the static pressure experienced by submerged mammals. We translate such a static pressure to the dynamic pressure of a falling drop, given by $P = \frac{1}{2}\rho U^2$ where P is the pressure and U is the liquid velocity. It would therefore be reasonable that the physical properties resisting infiltration by static pressure are the same as those resisting impact velocity or dynamic pressure represented by Re. The higher P_{crit}, the greater the ability of mammalian fur to retain an air layer, which should translate, in the case of mammals experiencing rainfall, to a higher k_2. Within the Π-group framework, this implies that the dimensionless dry-zone thickness $\Pi_4 = k_2/D_0$ should increase with Π_7 (underfur density), Π_{10} (distal diameter), and Π_{11} (roughness), and decrease with increasing Reynolds number (i.e. increasing inertial forcing). To encode these monotonic trends in a compact form, we again assume a separable power-law dependence,

$$\Pi_4 \propto \Pi_1^{\beta_1}\Pi_7^{\beta_7}\Pi_{10}^{\beta_{10}}\Pi_{11}^{\beta_{11}}, \tag{5}$$

where $\Pi_1 = \mu/(\rho D_0 U)$ is the reciprocal Reynolds number. Choosing $\beta_1, \beta_7, \beta_{10}, \beta_{11} > 0$ so that Π_4 increases with viscosity, underfur density, diameter, and roughness leads to the scaling

$$\Pi_4 \sim \Pi_1\Pi_7\Pi_{10}\Pi_{11}, \tag{6}$$

which, after substituting the dimensional definitions, produces

$$\frac{k_2}{D_0} \sim \frac{\delta_u d_3 r_g}{Re} = \frac{\mu\delta_u d_3 \tilde{r}_g}{\rho U D_0}. \tag{7}$$

A plot of k_2 versus $\mu\delta_u d_3\tilde{r}_g/\rho U$ is shown in figure 6(d). As $\mu\delta_u d_3\tilde{r}_g/\rho U$ increases past a value of 1.5×10^{-6} mm, asymptotic growth of k_2 can be observed, where any further increase in $\mu\delta_u d_3\tilde{r}_g/\rho U$ no longer increases k_2. Below such minimum threshold value, the fur properties are insufficient to establish a dry zone layer as in the case of the gray wolf with $\mu\delta_u d_3\tilde{r}_g/\rho U = 1.2 \times 10^{-6}$ mm.

Unsurprisingly, the dry zone at saturation is present in semi-aquatic mammals, such as the beaver, sea otter, and mink, given the air-entrapping properties when submerged [1]. What is remarkable is that the moose, a terrestrial mammal, exhibits a dry

zone at saturation as shown in figure 6(a). Some terrestrial mammals have fur properties close enough to semi-aquatic mammals to allow them to have an insulating dry layer at saturation [1]. Whereas mammals living in cold environments use fur for insulation and retaining body heat [43], mammals living in hot environments such as elk regulate temperature by allowing water to reach their skin for evaporative cooling [44]. Mammals whose fur serves a thermoregulatory function in multiple environments, such as moose, tend to be less effective for thermoregulation in each environment compared with mammals specialized in one environment [2]. The existence of the insulating air layer in moose likely stems from their habit of aquatic foraging and diving [45], where the air layer would act as useful thermal insulation. Zebras, native to the hot African plains, have adopted various methods to regulate their body temperature through evaporative cooling. Unlike mammals that seek thermal insulation in water to stay warm, the primary objective of zebras is to cool down, which explains why zebras have $k_1 = L$ and $k_2 = 0$ from our experiments. Zebras primarily cool themselves through sweat [46]. Their distinctive black and white stripes also play a significant role in thermoregulation [46]. The stripes create small-scale air currents on the surface of their bodies, which helps dissipate heat more effectively. Such a combination of behaviors and physical adaptations enables zebras to manage their body temperature efficiently in their natural environment. Gray wolves live in a wide range of habitats and live in North America, Europe, and Asia, and shed from April to June, when they lose their thick winter coat [42]. The sparse summer coat results in the lack of dry zone at saturation for the gray wolf pelt as shown in figures 6(a) and (d) and the high penetration depth in figure 6(c). Without the winter coat, gray wolves do not possess the underfur density required to maintain dry skin.

The rate of saturation is determined by the ability of the fur to dissipate the kinetic energy of impacting drops. The greater the viscous dissipation, the fewer drops are needed for the dry zone saturation thickness to be achieved. The importance of viscous forces is captured by the Ohnesorge number $Oh = \sqrt{We}/Re$. The guard hairs absorb the kinetic energy of the drop before it reaches the underfur [20, 26]. A thicker guard hair increases the surface area and likelihood of contact with liquid, forcing the fluid to spread through the interstices of the mammalian fur as the liquid infiltrates and enhancing viscous dissipation. Consequently, the rate of approach to saturation should increase with viscous effects and decrease when inertial and capillary forces dominate, which is naturally expressed through the Ohnesorge number $Oh = \sqrt{We}/Re$. In terms of the Π groups, this suggests that the dimensionless saturation rate $\Pi_5 = \lambda$ should grow with Π_1 (reciprocal Reynolds number) and decrease with $\Pi_2^{1/2}$ and Π_{10} (thicker hairs yielding slower saturation). We therefore adopt a separable power-law of the form

$$\Pi_5 \propto \Pi_1^{\gamma_1} \Pi_2^{\gamma_2} \Pi_{10}^{\gamma_{10}}, \tag{8}$$

and choose exponents consistent with these monotonic trends and with an overall Oh^{-1} dependence of λ. This leads to the scaling

$$\Pi_5 \sim \frac{\Pi_1}{\Pi_2^{1/2} \Pi_{10}}, \tag{9}$$

from which equation (10) follows directly after substitution:

$$\lambda \sim \frac{\sqrt{We} D_0}{Re d_3} = \left(\frac{d_3}{Oh D_0} \right)^{-1}. \tag{10}$$

A thicker guard hair narrows the interstices through which liquid must pass, so each drop traverses a longer path to reach a steady-state configuration within the fur before the next impact arrives. So long as successive impacts do not encroach on the impact timescale D_0/U, λ would be independent of time between impacts. Because the approach to local equilibrium is slower per drop, more drops are required to drive the system to its saturated penetration depth. Thus, λ decreases with increasing d_3. The hairs in our fur samples lay on top of one another and the geometry created by the touching hairs is determined by their diameter whereas hair density simply changes the thickness of the fur, L. Thus, density increases the dry zone thickness k_2 but does not affect λ. Past a certain density, unless the fibers are made longer to lie flat, further increasing the density will cause the hairs to stand erect, which will alter the penetration dynamics [21]. A plot of λ versus d_3/OhD_0 is shown in figure 6(e) and a plot of λ versus δ_g is shown in figure S2 of the supplementary document. λ exhibits a decay with increasing d_3/OhD_0, suggesting diminishing returns beyond a certain distal diameter shown in figure 6(e). The values of L, k_1, k_2, λ, and non-dimensional functional groups corresponding to the plots in figure 6 are listed in table 3.

The fits predicted in equations (4), (7) and (10) using our Buckingham-Pi analysis with their corresponding R^2 value are shown in black. In equation (4), we expect the penetration depth k_1 to be finite when fur density approaches zero. Thus, the model used in figure 6(c) is of the form $y = c/(x - x_0)$ where c and x_0 are constant fitting parameters. When fur density approaches infinity, the fur will act as a solid surface and prevent penetration so that k_1 will approach zero. In equation (7), we expect the dry zone k_2 to vanish as fur density approaches zero. Thus, the model used in figure 6(d) is of the form $y = cx$ where c is a constant fitting parameter. In equation (10), we expect the dry zone decay rate λ to approach zero as the hair diameter approaches infinity as the liquid body

Table 3. Values of L, k_1, k_2, λ, and non-dimensional functional groups in figure 6: $F_1 = (\delta_g \delta_u L_g L_u d_3 \tilde{r}_g / We^{3/4})^{-1}$, $F_2 = \mu \delta_u d_3 \tilde{r}_g / \rho U D_0$, and $F_3 = d_3 / Oh D_0$.

Mammal	L [mm] ($N = 3$)	k_1 [mm]	k_2 [mm]	λ	F_1 ($N = 3$)	F_2 [$\times 10^{-6}$] ($N = 3$)	F_3 ($N = 3$)
Gray wolf	36.6 ± 1.3	32.3	0.0	0.1	0.32 ± 0.12	0.3 ± 0.1	19.0 ± 0.4
Moose	20.6 ± 1.2	20.6	5.3	0.3	0.28 ± 0.04	0.5 ± 0.2	12.2 ± 0.3
Beaver	29.5 ± 0.7	15.1	9.0	0.1	0.87 ± 0.31	2.7 ± 0.9	22.5 ± 0.2
Mink	21.8 ± 0.5	20.7	6.9	0.2	0.04 ± 0.01	1.3 ± 0.5	15.6 ± 0.2
Sea otter	23.7 ± 1.1	19.0	9.0	0.2	0.21 ± 0.05	5.6 ± 0.8	17.2 ± 0.5

will need to travel an infinitely long distance along the hair diameter. As the hair diameter approaches zero, the decay rate will approach the constant value equal to the decay rate of a drop impacting a wet surface. Thus, the model used in figure 6(e) is of the form $y = c/(x - x_0)$ where c and x_0 are constant fitting parameters. Although the functional groups provide a simple relationship between fur parameters and experimental coefficients k_1, k_2, and λ, we acknowledge that some of the predictions set forth by equations (4), (7) and (10) do not fit experimental data well. Upon inspection, alternative fits better align with our data in figures 6(d) and (e). For instance, we plot an exponential fit ($y = c_1 - c_1 e^{-c_2 x}$; c_1 and c_2 are constant fitting parameters) for figure 6(d) and a linear fit ($y = c_1 x + c_2$; c_1 and c_2 are constant fitting parameters) for figure 6(e) which have improved R^2 values, shown in red. Investigating the physical basis for such alternative fits is an area for futurework.

In figure S3, S5, and S6 of the supplementary document, we plot the dry zone thickness coefficients k_1, k_2, and λ against each variable constituting their respective functional group in equations (4), (7) and (10). Though a few variables show a clear trend with the dry zone thickness coefficients, many variables do not show a clear trend; remarkably, when combined, these variables form a discernable trend with the dry zone thickness coefficients as shown in figure 6(c)–(e). To understand if all these variables are important in the functional groups, it is worth investigating if any of these variables are correlated. We show the pairplots of the functional group variables in figure S4, figure S5, and figure S6 of the supplementary document where it becomes clear that there is no strong correlation between variables.

We also found that the advancing, equilibrium, and receding contact angles as well as the contact angle hystereses do not play a role in the functional group for k_1, k_2, or λ. We show a plot of k_1, k_2, and λ against the advancing contact angle in figure S7 of the supplementary document. It is clear that any monotonic trend is absent in figure S7. Notably, since the contact angles, contact angle hystereses, or cosines thereof are dimensionless, their inclusion in our already dimensionless groups makes no improvement. In section 3, we confirmed the hydrophilicity of mammalian guard hair and hydrophobicity of mammalian underfur hair, the combined wettability that was previously hypothesized to optimally resist penetration. Although this dual wettability is essential for the formation of the dry zone, our findings suggest that the quantitative variation of the dry zone across species is governed by the geometric properties of the pelage rather than by inter-specific differences in contact angle.

The exponential model and associated non-dimensional groups provide a framework for designing bio-inspired materials and engineering surfaces with tailored interactions with moisture. Our model indicates that tuning fiber density, length, diameter, and surface roughness governs whether a hairy surface preferentially retains or sheds water. Whereas natural systems exploit both repelling and capture regimes, they serve distinct functions: water capture is seen in spider-silk- or cactus-spine-inspired structures for droplet collection and transport [47–49], whereas water repellency is a hallmark of fur, which traps air to keep mammals insulated, dry, and protected from abrasion. Such biological strategies highlight opportunities for engineered fur-like surfaces where a single layer provides multi-functionality such as thermal insulation, water resistance, and mechanical robustness without requiring composite construction such as coated metal with added insulation. Importantly, the governing structural parameters are manufacturable: fiber density and diameter can be controlled through electrospinning [50], whereas surface roughness can be tuned via laser texturing [51] or coatings [52]. Thus, the dimensionless groups we propose offer practical design guidelines that connect biological inspiration, scalable fabrication methods, and multifunctional moisture-management surfaces. There remains the question of how generalizable our results are to pelts not represented here, for which there are thousands, and imaginable synthetic arrays of comparable density. We posit that the scaling predictions of equations (4), (7) and (10) are robust, but indeed more tests are needed to confirm the water repellency they predict. Indeed the morphology of pelts in terms of length, density, curliness, fiber size, etc is vast.

5. Conclusion

In this work, we prove the existence of an insulating air layer or a 'dry zone' in terrestrial and semi-aquatic mammals when exposed to sequential raindrops. Until now, studies of the interaction between water and fur have been limited to submerged furs and mammalian shaking to dry. This study is the first to probe the penetration of falling water, in contrast to swimming, into a mammalian pelt. Our work suggests that most mammals can stay dry even during the most violent rainfall through their fur architecture. Denser, longer, and thicker hairs generally improve resistance to raindrop penetration, as expected. The roughness of the guard fur is an additional parameter that improves penetration resistance. Although semi-aquatic mammals achieve the thickest dry zones, we show that some terrestrial mammals, such as moose, achieve a non-zero dry zone. We propose an exponential decay model for the dry zone thickness as a function of the number of drops with coefficients that pertain to the penetration depth at saturation, the dry zone thickness at saturation, and the rate of saturation relative to the number of drops. We confirm the hydrophilicity of mammalian guard hair and hydrophobicity of mammalian underfur hair, the combined wettability that was previously hypothesized to optimally resist penetration. Although this dual wettability is essential for the formation of the dry zone, the quantitative variation of the dry zone across species is governed by the geometric properties of the pelage rather than by inter-species differences in contact angle. A comparison of fresh and taxidermied pelt samples suggests that the wettability of mammalian hair is due to its microstructure and not any oils or coatings originating from the mammalian skin. Future works could consider more mammalian species in a wider range of habitats, drop impact speeds, and measure missing parameters such as underfur diameter and roughness. These parameters may provide additional insight into the physical mechanisms governing the system. Incorporating underfur diameter and roughness could enhance the completeness of the dimensionless groups and further improve our models across a broader range of mammalian species or environmental conditions.

This study links the physics of rainfall infiltration in real mammalian pelts to the broader body of work on synthetic fiber arrays. Although idealized horizontal and vertical fiber arrays have shown how wettability, density, and orientation influence dynamic penetration, and although circular cross-sections have been shown to enhance penetration by suppressing lateral spreading, real pelts behave fundamentally differently. Across semi-aquatic and terrestrial species, we observe an exponential limiting of the penetration depth and a persistent dry insulating zone. Such behaviors are not reproducible in synthetic arrays, including circular geometries. Our findings in this work demonstrate that the coupled effects of mixed guard-underfur layers, natural tapering, density gradients, and hierarchical roughness endow biological fur with a robustness to dynamic wetting that synthetic systems cannot yet match.

Acknowledgments

This research was partially funded by the National Science Foundation (CMMI 1825801 and CBET 2205558). We thank Dr Sarah C. Linn-Peirano from the Department of Biomedical and Diagnostic Sciences, College of Veterinary Medicine at the University of Tennessee for helping us collect fresh domestic cat fur samples.

Data availability statement

The data that support the findings of this article are openly available in Zenodo at https://doi.org/10.5281/zenodo.19632181 [53].

Author contributions

Gene Patrick S Rible 0000-0002-4404-3040
Conceptualization (supporting), Data curation (lead), Formal analysis (lead), Investigation (lead), Methodology (equal), Project administration (lead), Resources (supporting), Software (supporting), Supervision (lead), Validation (equal), Visualization (equal), Writing – original draft (equal), Writing – review & editing (equal)

John M Wylie 0009-0005-0452-5650
Data curation (equal), Formal analysis (equal), Investigation (equal), Methodology (equal), Project administration (supporting), Resources (equal), Software (lead), Supervision (supporting), Validation (equal), Visualization (equal), Writing – original draft (supporting), Writing – review & editing (supporting)

Braeden K Elbers
Data curation (equal), Methodology (equal), Project administration (equal), Resources (equal), Software (equal), Supervision (supporting)

David Job Dooley
Data curation (supporting), Methodology (equal), Project administration (supporting), Resources (equal), Software (equal), Supervision (supporting)

Cora L Thomas
Conceptualization (supporting), Data curation (equal), Formal analysis (equal), Investigation (supporting), Methodology (equal), Resources (supporting), Writing – original draft (supporting)

Andrew K Dickerson 0000-0003-1220-1048
Conceptualization (equal), Formal analysis (equal), Funding acquisition (lead), Methodology (supporting), Resources (equal), Validation (equal), Writing – review & editing (supporting)

References

[1] Ivlev Y F 2019 Biomechanical analysis of fur as a tool for study of thermal insulation in semi-aquatic mammals *Biol. Bull.* **46** 763–79
[2] Liwanag H E, Berta A, Costa D P, Abney M and Williams T M 2012 Morphological and thermal properties of mammalian insulation: the evolution of fur for aquatic living *Biol. J. Linn. Soc.* **106** 926–39
[3] Yochem P K and Stewart B S 2009 Hair and fur *Encyclopedia of Marine Mammals* (Elsevier) pp 529–30
[4] Nasto A 2018 *Hairy interfaces PhD Thesis Massachusetts* Institute of Technology
[5] Myhrvold C L, Stone H A and Bou-Zeid E 2012 What is the use of elephant hair? *PLoS One* **7** 1–6
[6] Ensikat H J, Ditsche-Kuru P, Neinhuis C and Barthlott W 2011 Superhydrophobicity in perfection: the outstanding properties of the lotus leaf *Beilstein J. Nanotechnol.* **2** 152–61
[7] Evans C A L and Smith D 1956 Sweating responses in the horse *Proc. R. Soc. B* **145** 61–83
[8] Mitchell M and Tully T N 2016 *Chapter mammals Current Therapy in Exotic Pet* Practice (Elsevier Health Sciences)
[9] Landreneau E B 2011 *Scales and Scale-Like Structures* (Texas A & M University)
[10] Mahal G S, Johnston A and Burns R H 1951 Types and dimensions of fiber scales from the wool types of domestic sheep and wild life *Text. Res. J.* **21** 83–93
[11] van Deijnen T 2012 A classification of scales on hair
[12] Zafarina Z and Panneerchelvam S 2009 Analysis of hair samples using microscopical and molecular techniques to ascertain claims of rare animal species *Malays. J. Med. Sci. MJMS* **16** 35
[13] Deedrick D and Koch S 2004 Microscopy of hair part ii: A practical guide and manual for animal hairs *Forensic Sci. Commun.* **6** 13–27
[14] Hicks J W 1977 *Microscopy of Hairs: a Practical Guide and Manual* (Department of Justice, Federal Bureau of Investigation)
[15] Krsmanovic M, Ali H, Biswas D, Ghosh R and Dickerson A K 2022 Fouling of mammalian hair fibres exposed to a titanium dioxide colloidal suspension *J. R. Soc. Interface* **19** 20210904
[16] Deng Y, Peng C, Dai M, Lin D, Ali I, Alhewairini S S, Zheng X, Chen G, Li J and Naz I 2020 Recent development of super-wettable materials and their applications in oil-water separation *J. Clean. Prod.* **266** 121624
[17] Krupin K Fur keeps heat in and cold water out
[18] Weisel J W, Nagaswami C and Peterson R O 2005 River otter hair structure facilitates interlocking to impede penetration of water and allow trapping of air *Can. J. Zool.* **83** 649–55
[19] Sokolov V E 2023 *Mammal Skin* vol 37 (University of California Press)
[20] Rible G P S, Spinazzola M A I, Jones R E I, Constantin R U, Wang W and Dickerson A K 2024 Dynamic drop penetration of horizontally oriented fiber arrays *Langmuir* **40** 13339–54
[21] Rible G P S, Chakpuang V, Holihan A D, Sebek H P, Osman H H, Brown K R, Wang W and Dickerson A K 2025 Dynamic drop penetration of vertically oriented fiber arrays *Phys. Fluids* **37** 022108
[22] Kokshaysky N V 1999 The water impermeability of discontinuous animal integuments *Zh. Obshch. Biol.* **60** 376–93
[23] Wu T 1980 On the scale effect for the movement of aquatic animals *Biogidrodinamika Plavaniya i Poleta (Biohydrodynamics of Swimming and Flying)* (Mir) pp 79–112
[24] Lighthill D 1980 Aerodynamic aspects of animal flight *Biogidrodinamika Plavaniya i Poleta (Biohydrodynamics of Swimming and Flying)* (Mir) pp 9–78
[25] Sedov L I 1980 *Metody Podobiya i Razmernosti v Mekhanike (Methods of Similarity and Dimensionality in Mechanics)* 10th edn (Nauka)
[26] Rible G P S, Soto A, Shome R C and Dickerson A K 2025 Sequential drop impacts onto horizontal fiber arrays *Phys. Fluids* **37** 072128
[27] Rible G P S, Raza S J, Boger J H, Osman H H, Holihan A D, Elbers B K, Brown K R, Schenck C M, Reed B J and Dickerson A K 2025 Cross-sectional circularity promotes dynamic drop penetration of horizontal fiber arrays *Phys. Fluids* **37** 122110
[28] Meng Q, Wang Q, Liu H and Jiang L 2014 A bio-inspired flexible fiber array with an open radial geometry for highly efficient liquid transfer *NPG Asia Mater.* **6** e125
[29] Gunn R and Kinzer G D 1949 The terminal velocity of fall for water droplets in stagnant air *J. Meteorol.* **6** 243–8
[30] Popov Y O 2005 Evaporative deposition patterns: Spatial dimensions of the deposit *Phys. Rev.* E **71** 036313
[31] Washburn E W 1921 The dynamics of capillary flow *Phys. Rev.* **17** 273–83
[32] Krsmanovic M, Ghosh R and Dickerson A K 2023 Fur flutter in fluid flow fends off foulers *J. R. Soc. Interface* **20** 20230485
[33] Dickerson A K, Mills Z G and Hu D L 2012 Wet mammals shake at tuned frequencies to dry *J. R. Soc. Interface* **9** 3208–18
[34] Koch S 2020 Splitting hairs (and fibers): 4 cross-sectioning methods (available at: www.mccrone.com/mm/splitting-hairs-4-methods-of-cross-sectioning/) (Accessed 04 June 2025)
[35] Menezes P L, Kishore and Kailas S V 2008 Influence of roughness parameters on coefficient of friction under lubricated conditions *Sadhana* **33** 181–90
[36] Environmental Literacy Council, n.d. What is the function of the guard hair? (Accessed 15 April 2025)
[37] Eriten M, Polycarpou A A and Bergman L A 2011 Surface roughness effects on energy dissipation in fretting contact of nominally flat surfaces *J. Appl. Mech., Trans. ASME* **78** 021011
[38] Demonti I 2023 *Sheepology* (Chronicle Books)
[39] Starov V, Zhdanov S, Kosvintsev S, Sobolev V and Velarde M 2003 Spreading of liquid drops over porous substrates *Adv. Colloid Interface Sci.* **104** 123–58
[40] Xu L, Ji W, Lu J, Li Y, Hao J, Hu G and Floryan J M 2021 Droplet impact on a prewetted mesh *Phys. Rev. Fluids* **6** L101602
[41] Sedlaček M, Podgornik B and Vižintin J 2008 Influence of surface preparation on roughness parameters, friction and wear *Wear* **266** 482–7
[42] Darimont C T and Paquet P C 2000 The gray wolves (Canis lupus) of British Columbia's coastal rainforests: findings from year 2000 pilot study and conservation assessment Technical Report (Raincoast Conservation Society)
[43] Scholander P, Walters V,Hock R and Irving L 1950 Body insulation of some arctic and tropical mammals and birds *Biol. l Bull.* **99** 225–36

[44] Mitchell D, Snelling E P, Hetem R S, Maloney S K, Strauss W M and Fuller A 2018 Revisiting concepts of thermal physiology: predicting responses of mammals to climate change *J. Anim. Ecol.* **87** 956–73
[45] Márquez S, Pagano A S, Mongle C S, Albertine K H and Laitman J T 2019 The nasal complex of a semiaquatic artiodactyl, the moose (alces alces): is it a good evolutionary model for the ancestors of cetaceans? *Anat. Rec.* **302** 667–92
[46] Cobb A and Cobb S 2019 Do zebra stripes influence thermoregulation? *J. Nat. Hist.* **53** 863–79
[47] Zheng Y, Bai H, Huang Z, Tian X, Nie F, Zhao Y, Zhai J and Jiang L 2010 Directional water collection on wetted spider silk *Nature* **463** 640–3
[48] Ju J, Bai H, Zheng Y, Zhao T, Fang R and Jiang L 2012 Cactus stem hairs and spines: An efficient fog collection system *Nat. Commun.* **3** 1247
[49] Tian Y and Wang L 2018 Bioinspired microfibers for water collection *J. Mater. Chem. A.* **6** 18766–81
[50] Hernandez J L *et al* 2022 Scalable electrospinning methods to produce high basis density fiber materials *Front. Biomater. Sci.* **1928537** 928537
[51] Zhou J, Wu J, Tang S and Li Y 2025 Review of laser texturing technology for surface protection and functional regulation of aluminum alloys: wettability, anti-icing, corrosion resistance and wear resistance *Coatings* **15** 567
[52] Shigrekar M and Amdoskar V 2024 A review on recent progress and techniques used for fabricating superhydrophobic coatings derived from biobased materials *RSC Adv.* **14** 32668–99
[53] Rible G P and Wylie J M 2026 Supplementary Data for our paper entitled "Fur roughness, density, and length reduce raindrop penetration of mammalian pelts" *Zenodo* (https://doi.org/10.5281/zenodo.19632181)